Spin-squeezing-enhanced optical lattice clocks with 10^{-19}-level differential frequency stability at the averaging time of 1 s

Deshui Yu[1,2,*] Jia Zhang,[3,*] Tongyan Xia[1,2] Shougang Zhang,[1,2,4] Tiantian Shi,[5,6,†] and Jingbiao Chen[3,7]

[1]*National Time Service Center, Chinese Academy of Sciences, Xi'an 710600, China*
[2]*Key Laboratory of Time Reference and Applications, Chinese Academy of Sciences, Xi'an 710600, China*
[3]*State Key Laboratory of Advanced Optical Communication Systems and Networks, Institute of Quantum Electronics, School of Electronics, Peking University, Beijing 100871, China*
[4]*University of Chinese Academy of Sciences, Beijing 100049, China*
[5]*School of Integrated Circuits, Peking University, Beijing 100871, China*
[6]*National Key Laboratory of Advanced Micro and Nano Manufacture Technology, Beijing 100871, China*
[7]*Hefei National Laboratory, Hefei 230088, China*

(Received 31 March 2024; accepted 10 June 2024; published 1 July 2024)

Many-body entangled states allow precision measurement beyond the standard quantum limit. Yet they have not been effectively exploited in optical lattice clocks except for proof-of-principle demonstrations. Under the current experimental conditions, taking into account the lattice perturbation, atom-atom interactions, and local oscillator noise, we theoretically evaluate the performance of spin-squeezing-based shallow-lattice Yb optical clocks. The numerical simulation shows that the stability of differential frequency comparison between two Yb ensembles in squeezed spin states potentially accesses the 10^{-19} level at the averaging time of 1 s. The resultant Wineland parameter may be as low as $\xi_{\mathrm{W}}^2 = 0.027$, corresponding to a reduction of averaging time by a factor of 37, and is limited by the collision-induced degradation of spin squeezing. The metrological gain provided by spin squeezing opens up new opportunities for precision measurement and fundamental physics.

DOI: 10.1103/PhysRevA.110.013102

I. INTRODUCTION

Substantial progress has been made in recent years on optical lattice clocks, significantly advancing precision measurement [1]. Clock uncertainty at the 10^{-18} level [2,3] allows gaining new insights into many-body physics [4,5], tighter limits on fundamental constant variation [6], ultralight dark matter, and gravitational waves [7]. Additionally, the careful evaluation of electric-quadrupole, magnetic-dipole, and hyperpolarizabilities and employing lattice lasers with substantially filtered background spectra have pushed the uncertainty of lattice-induced light shifts down to the 10^{-19} level [8–11]. Moreover, operating clocks in shallow lattices minimizes Raman scattering in upper clock states [12], thereby extending the interrogation time up to tens of seconds [13,14] and raising the clock duty cycle. Further, subtle engineering of the Hamiltonian of lattice-trapped atoms tunes the density shift to zero [15], leading to a differential frequency uncertainty at the 10^{-21} level over the averaging time of 10^2 h, which enables resolving the gravitational redshift across a millimeter-scale atomic sample [14].

Conventional optical lattice clocks are built upon N uncorrelated probe particles (atoms and ions). The corresponding uncertainty of the clock phase measurement is bounded by the standard quantum limit (SQL) that arises from the quantum projection noise (QPN) of independent particles in coherent spin states (CSSs) [16,17], $(\Delta\phi)_{\mathrm{SQL}} = N^{-0.5}$ (Fig. 1). Employing nonclassical spin states of particles may beat the SQL [18]. The one-axis twisting based on photon-mediated [19], Rydberg-dressed [20], and power-law [21] interactions between particles is usually utilized to carry out spin squeezing. The resultant measurement uncertainty based on squeezed spin states (SSSs) scales as $(\Delta\phi)_{\mathrm{SSS}} = N^{-0.83}$ (see below). In addition, measurement-based spin squeezing was recently demonstrated on state-of-the-art optical clocks by means of cavity quantum electrodynamics [22,23]. Indeed, the true fundamental limit to the phase resolution is imposed by the Heisenberg uncertainty principle [24], i.e., the Heisenberg limit $(\Delta\phi)_{\mathrm{HL}} = N^{-1}$, and can be reached using maximally entangled states (MESs). This has been verified through a quantum network composed of a few entangled optical clocks [25]. However, creating large-scale MESs that are highly desired for metrological applications is still challenging [26–28].

The performance of a many-body optical clock has not yet reached the SQL due to the technical noise that results from the interrupted interrogation of particles, known as the Dick effect [29]. Thanks to the substantial reduction of the thermal Brownian noise in local oscillators [30,31], the Dick-effect-limited instability of an optical clock may reach the low $10^{-17}/\sqrt{\tau}$ level for an averaging time τ [32], but still lies above the SQL. Fortunately, the absolute frequency measurement of optical clocks is not essential for many practical applications such as testing general relativity [33] and engineering interparticle interactions [15]. All the necessary information can be directly derived from the differential frequency

*These authors contributed equally to this work.
†Contact author: tts@pku.edu.cn

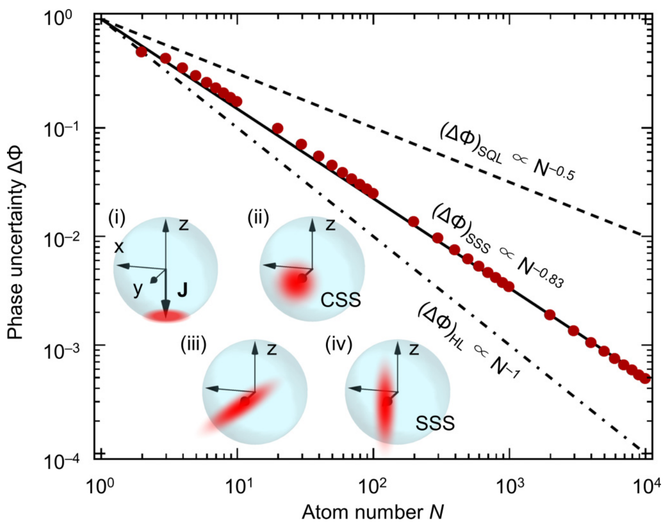

FIG. 1. Phase measurement uncertainty $\Delta\phi$ in the Ramsey spectroscopy as a function of the particle number N. Circles: numerical results based on the one-axis-twisting spin squeezing. Solid line: curve fitting. Inset: steps of creating SSSs via the one-axis twisting.

measurement between two probe particle systems, where the rejection of the Dick noise leads to a clock comparison limited by the QPN [34]. Recently, a synchronous frequency comparison demonstrated the unprecedented $10^{-18}/\sqrt{\tau}$ level [14].

All of the above progress paves the way toward a spin-squeezing-enhanced synchronous frequency comparison beyond $10^{-18}/\sqrt{\tau}$. In this work, we investigate the potential frequency stability of the synchronous comparison between shallow-lattice Yb optical clocks using SSSs. The clock operation is numerically simulated, where the noise in the state-of-the-art local oscillator, lattice-induced light shifts of the clock transition, and atom-atom collisions are involved. It is found that the resultant differential frequency stability accesses the 10^{-19} level at the averaging time of 1 second, opening up new opportunities in quantum metrology and precision measurement.

II. SHALLOW-LATTICE Yb OPTICAL CLOCKS

As shown in Fig. 2(a), two laser sub-beams from an ultrastable local oscillator at 578 nm interact with two Yb ensembles, Yb-1 and Yb-2, respectively, in a synchronous manner. Two atomic ensembles are separately trapped in two one-dimensional (1D) optical lattices and have the same atom number N. The sub-beams are respectively locked to the $|g\rangle \equiv {}^1\mathrm{S}_0(F=\frac{1}{2}, M_F=-\frac{1}{2})$–$|e\rangle \equiv {}^3\mathrm{P}_0(F=\frac{1}{2}, M_F=\frac{1}{2})$ clock transition in Yb ensembles through two independent acousto-optic modulators, AOM-1 and 2. Here, F denotes the total angular momentum and M_F is the z-axis projection. Ramsey spectroscopy is applied to derive the laser frequency.

A. One-axis-twisting spin squeezing

The one-axis-twisting model is employed to implement spin squeezing of individual ensembles and the Ramsey interrogation is performed accordingly [19]. The specific procedure is summarized as follows (see the inset of Fig. 1): Two states, $|g\rangle$ and $|s\rangle \equiv {}^1\mathrm{S}_0(F=\frac{1}{2}, M_F=\frac{1}{2})$, of Yb form a spin

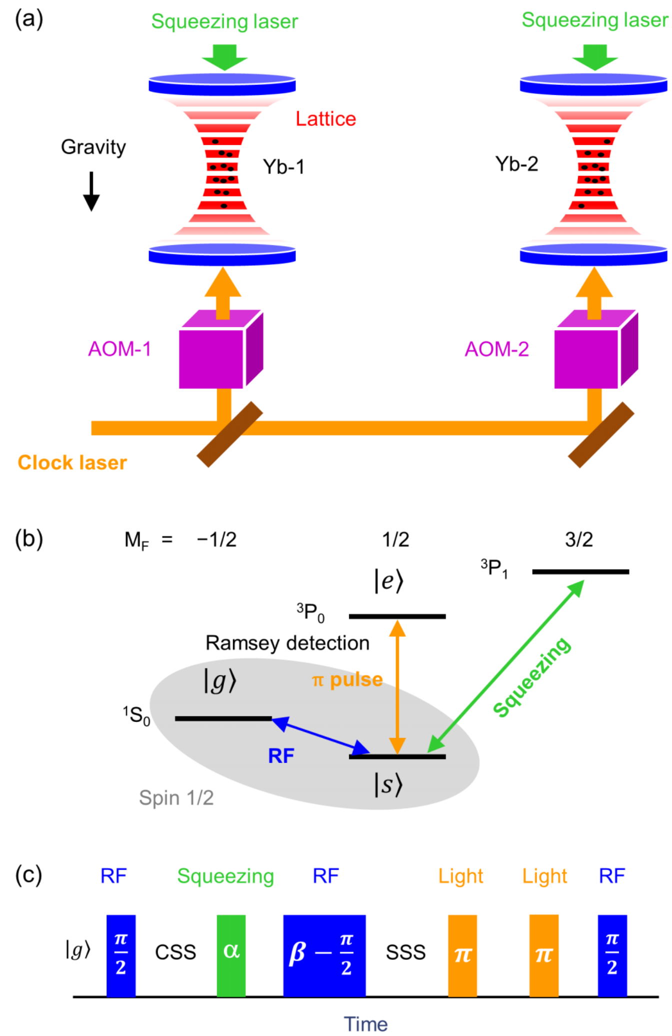

FIG. 2. Spin-squeezing-enhanced optical lattice clocks. (a) Clock scheme of synchronous frequency comparison. Two ensembles of Yb atoms are separately trapped in two 1D optical lattices and are interrogated by the same clock laser. (b) Energy-level structure of Yb atom. (c) Time sequence of clock cycle.

[Fig. 2(b)]. All atoms in an ensemble are initialized in $|g\rangle$. A radiofrequency (rf) $\frac{\pi}{2}$-pulse is resonantly coupled with the $|g\rangle$ - $|s\rangle$ transition, generating the CSS of the ensemble,

$$|\psi_{\mathrm{CSS}}\rangle = e^{-i\pi\hat{S}_x/2}\,\Pi_{\mathbf{m}} \otimes |g\rangle_{\mathbf{m}}\,, \tag{1}$$

as shown in Fig. 2(c). Here, $\mathbf{m}=(m_x, m_y, m)$ labels the motional state of a lattice-trapped fermionic atom that is localized on the mth lattice site and undergoes radial harmonic vibration with the quantum numbers $m_{u=x,y}$, and $\hat{S}_{u=x,y,z}$ are the total spin operators (see Appendix A). Then, an off-resonant light pulse drives the $|s\rangle$ - ${}^3P_1(F=\frac{3}{2}, M_F=\frac{3}{2})$ transition and the ensemble undergoes one-axis twisting evolution for a duration α. Another rf pulse is subsequently used to rotate the spin system around the y axis by an angle $(\beta-\frac{\pi}{2})$, resulting in the SSS of the ensemble

$$|\psi_{\mathrm{SSS}}\rangle = e^{-i(\beta-\pi/2)\hat{S}_y}e^{-i\alpha\hat{S}_z^2}\,|\psi_{\mathrm{CSS}}\rangle\,. \tag{2}$$

A light π pulse illuminates the ensemble, mapping all atoms in $|s\rangle$ to the upper clock $|e\rangle$ state. After a dark time T, a second light π pulse is launched to map the atoms in $|e\rangle$ back to $|s\rangle$. Finally, the other rf $\frac{\pi}{2}$-pulse resonantly drives the $|g\rangle$ - $|s\rangle$ transition and the projection measurement

$$p(\phi) = 1/2 + \langle\psi_f(\phi)|\,(\hat{S}_z/N)\,|\psi_f(\phi)\rangle \tag{3}$$

is performed on the ensemble that is in the state

$$|\psi_f(\phi)\rangle = e^{-i\frac{\pi}{2}\hat{S}_x} e^{-i\phi\hat{S}_z}\,|\psi_{\mathrm{SSS}}\rangle\,, \tag{4}$$

where ϕ accounts for the phase difference accumulated between the clock laser and the atomic clock transition over the dark period. The angles (α, β) are numerically determined according to the minimization of the phase measurement uncertainty

$$\Delta\phi = \Delta p/|\partial p/\partial\phi|, \tag{5}$$

with the variance of the projection measurement

$$(\Delta p)^2 = \langle\psi_f(\phi)|\,(\hat{S}_z/N)^2\,|\psi_f(\phi)\rangle - p^2. \tag{6}$$

The detailed theoretical description can be found in Appendix A and [35,36].

B. Coherence time of clock transition

Various noise sources disturb the $|g\rangle$ - $|e\rangle$ clock transition. It has been pointed out that, although the natural linewidth of the clock transition is as low as 8.3 mHz, the Raman scattering (e.g., ${}^3P_0 \rightarrow {}^3P_1$) of lattice photons strongly shortens the lifetime of $|e\rangle$ [37]. This issue can be addressed by operating the clock in a shallow lattice [38,39]. According to the experimental results in [37], the dependence of the coherence time τ_{coh} of the clock transition on the lattice potential U_0 is approximated by

$$\tau_{\mathrm{coh}}(u) = (2\pi \times 0.09\ \mathrm{mHz} \times u + 2\pi \times 8.3\ \mathrm{mHz})^{-1}, \tag{7}$$

with $u = U_0/E_R$, the photon recoil energy $E_R/h = 2.0$ kHz, and the Planck constant h.

The conventional lattice depth U_0 for the clock operation is hundreds of E_R, resulting in a τ_{coh} of the order of 1 s [19,40]. As the lattice depth is reduced down to $10E_R$, τ_{coh} approaches the natural lifetime of $|e\rangle$ [Fig. 3(a)], allowing a clock interrogation time limited by the local oscillator's coherence time and also enhancing the clock duty cycle. In addition, the main population peak of a lattice-trapped atom is over three orders of magnitude higher than that of nearest-neighbor sites. Thus, the strong Wannier-Stark localization of atoms is still maintained in the shallow lattice (see Appendix B).

It is worth pointing out that according to the recent achievements in shallow-lattice Sr optical clocks [10,14,15,22], shallow-lattice Yb optical clocks hold promising prospects, although the relevant practical clock operation has not been demonstrated yet.

C. Light shifts

The clock transition experiences lattice-induced light shift. The conventional magic wavelength of 759 nm, at which two clock states have the same dynamic electric-dipole polarizability [41], allows reducing the clock uncertainty induced by the lattice intensity fluctuations below 10^{-17} [3,6,42]. Further suppression of the light shift down to the 10^{-19}

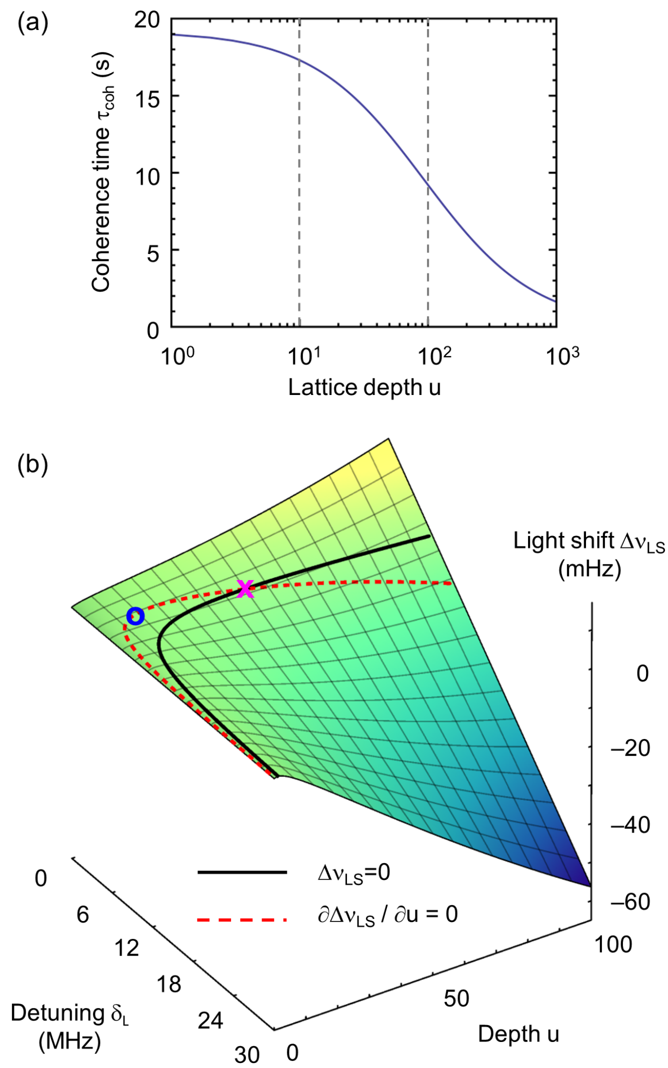

FIG. 3. (a) Dependence of the coherence time τ_{coh} of the clock transition on the lattice depth u for Yb lattice clocks. (b) Dependence of the light shift $\Delta\nu_{\mathrm{LS}}$ on the detuning δ_{L} of the lattice laser away from the conventional magic wavelength of 759 nm and the lattice depth u for Yb lattice clocks. The $\times$ symbol denotes the crossing point between $\Delta\nu_{\mathrm{LS}}(\delta_{\mathrm{L}}, u) = 0$ (solid) and $\frac{\partial}{\partial u}\Delta\nu_{\mathrm{LS}}(\delta_{\mathrm{L}}, u) = 0$ (dashed) curves. The $\circ$ symbol corresponds to the point $\frac{\partial}{\partial u}\Delta\nu_{\mathrm{LS}}(\delta_{\mathrm{L}}, u = 10) = 0$.

level relies on the careful evaluation of differential electric-quadrupole, magnetic-dipole, and hyperpolarizabilities [8,10]. In the clock operation, all atoms are usually prepared in the axial ground vibrational state. The dependence of the light shift $\Delta\nu_{\mathrm{LS}}(\delta_{\mathrm{L}}, u)$ of the clock transition on the small lattice laser detuning δ_{L} away from the conventional magic wavelength and u is derived as (see Appendix C)

$$\begin{aligned} h\Delta\nu_{\mathrm{LS}} = {} & \partial_\nu \Delta\tilde{\alpha}^{E1}\,\delta_L\,(\sqrt{pu}/2 - pu) - \Delta\tilde{\alpha}^{qm}\sqrt{pu}/2 \\ & - q\,\Delta\tilde{\beta}\,(3u/4p - u^{3/2}/\sqrt{p} + u^2), \end{aligned} \tag{8}$$

with $p = (1 + k_B T_r/U_0)^{-1}$, $q = (1 + 2k_B T_r/U_0)^{-1}$, the Boltzmann constant k_B, and the radial temperature T_r of atoms. The experimental results of the frequency derivative of the differential electric dipole ($E1$) polarizability $\Delta\tilde{\alpha}^{E1}$, the differential multipolar polarizability, and the differential hyperpolarizability between $|g\rangle$ and $|e\rangle$ are $\partial_\nu \Delta\tilde{\alpha}^{E1}/h = 25.74$ μHz/MHz, $\Delta\tilde{\alpha}^{qm}/h = -1027$ μHz, and $\Delta\tilde{\beta}/h = -1.194$ μHz, respectively [9]. In this work, we set $T_r = 0.2$ μK. Achieving such low radial temperature is feasible, although the practical implementation is complex [37,43].

In principle, the operational lattice detuning and depth should be set at the crossing point ($\delta_\mathrm{L} = 5.2$ MHz, $u = 43.1$) between the line for the vanishing of the light shift $\Delta\nu_\mathrm{LS} = 0$ and the line for minimizing the sensitivity of $\Delta\nu_\mathrm{LS}$ on lattice intensity fluctuations $\partial\Delta\nu_\mathrm{LS}/\partial u = 0$ (see Fig. 3) [8]. However, in order to operate the clock in a shallow lattice, we only focus on the latter condition at the cost of sacrificing the clock accuracy $\Delta\nu_\mathrm{LS} \neq 0$. Setting $u = 10$ gives the corresponding detuning $\delta_\mathrm{L} = 4.5$ MHz and the light shift $\Delta\nu_\mathrm{LS} = 0.8$ mHz (fractional shift of 1.5×10^{-18}). The uncertainty of $\Delta\nu_\mathrm{LS}$ can be less than 2 μHz (fractional uncertainty at the 10^{-21} level) by controlling the relative fluctuations of the lattice intensity within 10% and narrowing the lattice laser linewidth down to 10 kHz.

It is worth pointing out that the theoretical (analytic) model (8) for light shifts is based on an ideal, background-free lattice laser system. However, as illustrated in [11], a practical lattice laser relies on a tapered amplifier that contains a broadband background spectral component stemming from the amplified spontaneous emission (ASE), thereby resulting in unwanted residual light shifts. The ASE can be spectrally filtered using a volume Bragg grating, leading to an estimated fractional frequency shift at the 10^{-21} level for typical experimental conditions [11]. In addition, employing a titanium:sapphire laser for the optical trapping benefits from a spectral purity that well surpasses the tapered amplifier.

D. Blackbody radiation shift

Besides the lattice-induced light shift, the clock transition is also perturbed by the blackbody radiation (BBR), resulting in a shift [44,45]

$$\Delta\nu_\mathrm{BBR} = -(1.25\ \mathrm{Hz})(T/T_0)^4 - (21.9\ \mathrm{mHz})(T/T_0)^6 - (0.74\ \mathrm{mHz})(T/T_0)^8, \tag{9}$$

with the ambient temperature T and $T_0 = 300$ K. The first term on the right-hand side corresponds to the static contribution and the rest of the terms account for small dynamic corrections. By operating the clock in the cryogenically shielded environment with $T = 77$ K, the BBR shift can be reduced to $\Delta\nu_\mathrm{BBR} = -5.5$ mHz (fractional shift of 1.1×10^{-17}). Determining the temperature within an uncertainty of $\Delta T = 0.1$ K leads to a fractional BBR uncertainty of 6×10^{-20}. Cryogenic optical lattice clocks have been recently demonstrated with a clock uncertainty of a few millihertz [3].

III. COLLISIONAL EFFECTS

The remaining major source of the clock uncertainty is the collisional shift $\Delta\nu_\mathrm{CS}$ of the $|g\rangle$ - $|e\rangle$ clock transition that arises from the off-site s-wave and on-site p-wave interactions between atoms [15]. The atom-atom interactions mainly occur within the Ramsey dark period, during which the atoms are in the superposition state of $|g\rangle$ and $|e\rangle$. Here, we assume that all atoms in $|s\rangle$ are completely mapped into $|e\rangle$ using the light π pulses [Figs. 2(b) and 2(c)]. The collisional shift $\Delta\nu_\mathrm{CS}$ can be evaluated through numerical simulation.

Following the spin-1/2 model approximation [15,46–48], the interatomic collisions in an ensemble are governed by the operator

$$\hat{V} = \sum_{\mathbf{m}\neq\mathbf{m}'} \big[\kappa_{\mathbf{m}\mathbf{m}'} \hat{\mathbf{j}}_\mathbf{m} \cdot \hat{\mathbf{j}}_{\mathbf{m}'} + \chi_{\mathbf{m}\mathbf{m}'} \hat{j}^z_\mathbf{m} \hat{j}^z_{\mathbf{m}'} + \gamma_{\mathbf{m}\mathbf{m}'}\big(\hat{j}^z_\mathbf{m}\hat{n}_{\mathbf{m}'} + \hat{n}_\mathbf{m}\hat{j}^z_{\mathbf{m}'}\big)\big], \tag{10}$$

with $\kappa_{\mathbf{m}\mathbf{m}'} = B^{(eg)}_{\mathbf{m}\mathbf{m}'} - A_{\mathbf{m}\mathbf{m}'}$, $\chi_{\mathbf{m}\mathbf{m}'} = B^{(eg)}_{\mathbf{m}\mathbf{m}'} + B^{(gg)}_{\mathbf{m}\mathbf{m}'} - 2B^{(eg)}_{\mathbf{m}\mathbf{m}'}$, and $2\gamma_{\mathbf{m}\mathbf{m}'} = B^{(ee)}_{\mathbf{m}\mathbf{m}'} - B^{(gg)}_{\mathbf{m}\mathbf{m}'}$. Here, the off-site s-wave $A_{\mathbf{m}\mathbf{m}'}$ and on-site p-wave $B^{(uv)}_{\mathbf{m}\mathbf{m}'}$ $(u, v = e, g)$ interaction strengths depend on the overlaps between the $\mathbf{m}$ and $\mathbf{m}'$ motional states of atoms and the s-wave ($a^-_{eg} = -25a_0$ with the Bohr radius a_0 [49]) and p-wave ($b_{eg} = -74a_0$, $b^3_{ee} = 0.1b^3_{eg}$, and $b_{gg} \approx 0$ [49]) scattering lengths (see Appendix D). $\hat{\mathbf{j}}_\mathbf{m} = \hat{j}^x_\mathbf{m}\mathbf{e}_x + \hat{j}^y_\mathbf{m}\mathbf{e}_y + \hat{j}^z_\mathbf{m}\mathbf{e}_z$ corresponds to the angular momentum operator associated with the two-state ($|g\rangle$ and $|e\rangle$) atom in the $\mathbf{m}$ motional state and $\hat{n}_\mathbf{m}$ account for the atom number operator.

In the specific simulation, we numerically create the distribution of atoms over different $\mathbf{m}$ motional states for each clock cycle. The on-site atom number follows the Gaussian distribution (with the axial width of the atomic cloud L_z) along the lattice axis. The radial distribution of atoms on a lattice site over different quantum harmonic oscillators labeled by the indexes m_x and m_y obeys the Fermi-Dirac distribution (see Appendix D).

In the clock operation, all atoms are initially prepared in the lower clock state, i.e., spin-polarized fermions, substantially suppressing the s-wave collisions due to the Fermi statistics. In addition, as verified in [49,50] the s-wave interactions between Yb atoms on different lattice sites can be ruled out even when the probe beam is artificially misaligned (i.e., introducing the excitation inhomogeneity larger than the typical value). Therefore, here we only consider the on-site p-wave interactions, i.e., the pair of $\mathbf{m}$ and $\mathbf{m}'$ atoms in Eq. (10) should be on the same lattice site. Additionally, the p-wave scattering between on-site $|g\rangle$ and $|e\rangle$ atoms mainly contributes the collisional shift due to $|b^3_{eg}| \gg |b^3_{ee,gg}|$.

The collisional shift $\Delta\nu_\mathrm{CS}$ is evaluated using Ramsey spectroscopy. In the SSS-based Ramsey measurent, where the ensemble has been prepared in $|\psi_\mathrm{SSS}\rangle$ [Eq. (2)], the ensemble wavefunction evolves to

$$|\psi_f\rangle = e^{-i\frac{\pi}{2}\hat{S}_x}\hat{\pi}\, e^{-i\phi\hat{J}_z} e^{-i2\pi\hat{V}T/h}\hat{\pi}\,|\psi_\mathrm{SSS}\rangle\,, \tag{11}$$

after the second Ramsey $\frac{\pi}{2}$ pulse. Here, $\hat{J}_z = \sum_\mathbf{m} \hat{j}^z_\mathbf{m}$ and ϕ denotes the accumulated phase difference between the laser and the clock transition over the dark period. The $\hat{\pi}$ operator denotes the operation of completely mapping atoms between $|e\rangle$ and $|s\rangle$ using the light π pulses [Figs. 2(b) and 2(c)]. The fractional excitation of atoms is derived by $p = 1/2 + \langle\psi_f|\,(\hat{S}_z/N)\,|\psi_f\rangle$. The collisional shift $\Delta\nu_\mathrm{CS}$ is generally measured at the Ramsey excitation fraction of 0.5 through repeating the simulation process [Fig. 4(a)]. Equation (11) illustrates that the interatomic interactions (denoted by the symbol V) introduce extra phases to different collective spin states of atoms (see Appendix D). This not only induces the

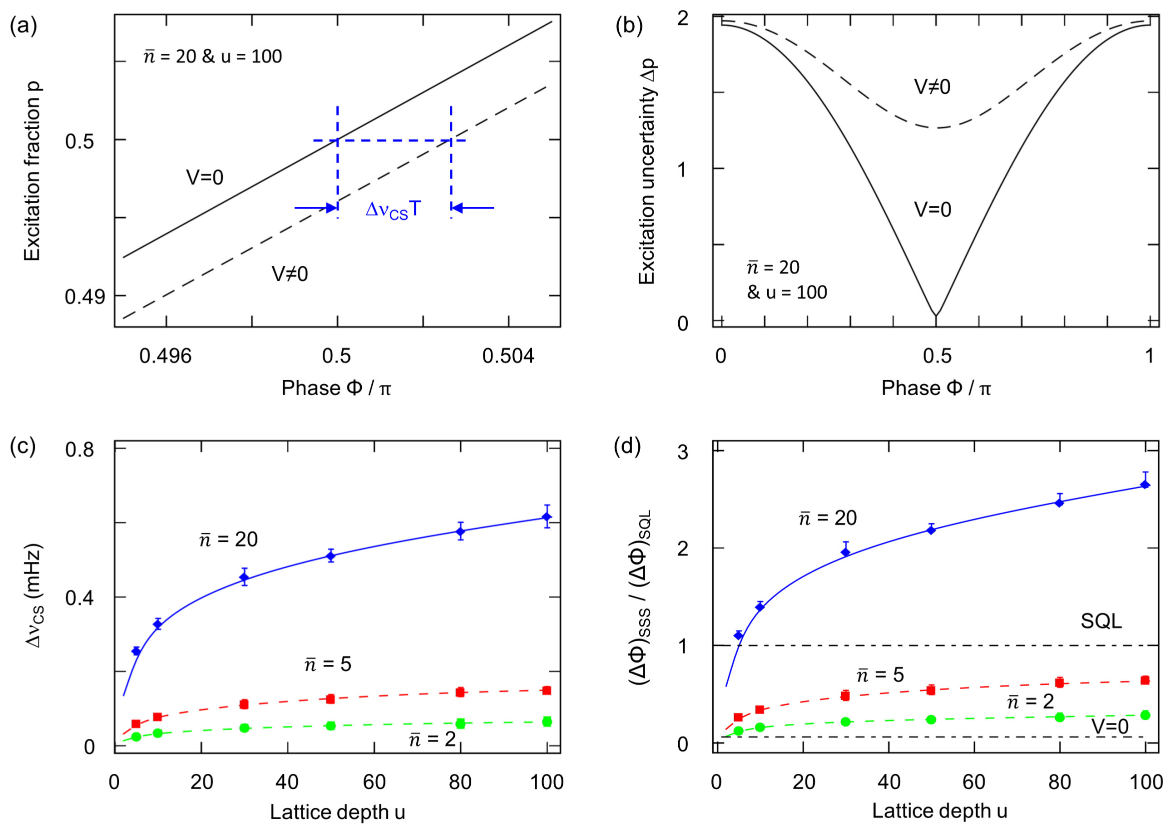

FIG. 4. Effects of atomic collisions on the SSS-based clock performance. (a) Excitation fraction p vs the phase difference ϕ between the two Ramsey pulses in the absence ($V = 0$) or presence ($V \neq 0$) of atom–atom interactions. The collisional frequency shift $\Delta\nu_{CS}$ is derived accordingly. p is evaluated by averaging over multiple Ramsey-measurement simulations. (b) Standard deviation (uncertainty) of the Ramsey excitation Δp. Δp is derived over multiple Ramsey-measurement simulations. Dependence of $\Delta\nu_{CS}$ (c) and the phase measurement uncertainty $\Delta\phi$ (d) on the lattice depth u for different average numbers $\bar{n}$ of on-site atoms. Symbols: numerical results. Lines: curve fitting. The SQL of the phase uncertainty in the absence of atom-atom interactions $V = 0$ is inserted in (d). For all plots, the trapped atoms has an average number $\bar{N} = 5000$ and a standard deviation $\sigma_N = 50$ and the radial temperature of atoms is $T_r = 0.2$ μK.

frequency shift of the clock transition $\Delta\nu_{CS}$ but also enhances the quantum fluctuations of the projection measurement $(\Delta p)^2 = \langle\psi_f|(\hat{S}_z/N)^2|\psi_f\rangle - p^2$ [Fig. 4(b)], degrading the degree of spin squeezing,

$$(\Delta\phi)_{SSS}(V = 0) = N^{-0.83} < (\Delta\phi)_{SSS}(V \neq 0). \tag{12}$$

The atom-atom interactions V depend strongly on the overlap of motional states of the on-site atoms. Decreasing the lattice depth u broadens the spatial distribution width of atoms in a pancake-shaped lattice site, suppressing the collisional shift $\Delta\nu_{CS}$ [Fig. 4(c)]. Additionally, the density of atoms decreases as the average number of atoms per site $\bar{n} = N\lambda_L/2L_z$ is reduced, where λ_L is the lattice wavelength and L_z is the axial width of the atomic cloud. In experiments, $\bar{n}$ may be adjusted through expanding the atomic cloud [51].

A few technical noise sources fluctuate the collisional shift. The atoms are prepared in the ground Wannier-Stark states in the axis direction and occupy different harmonic oscillators according to the Fermi distribution in the radial direction. The occupied radial states differ over clock cycles, leading to the uncertainty of the collisional shift. In addition, the lattice-trapped ensembles in different clock cycles may not have the same atom number. Furthermore, the on-site atom number varies over the lattice region due to the Gaussian distribution of the atomic cloud in the axial direction (see Appendix D). Under the typical experimental conditions, for example, the trapped atoms have an average number $\bar{N} = 5000$ and a standard deviation $\sigma_N = 50$ [34]. We set the on-site atom number as $\bar{n} = 2$ (the corresponding width of the ultracold cloud is approximately 1 mm) and the radial temperature of atoms at $T_r = 0.2$ μK. The numerical simulation gives $\Delta\nu_{CS} = 0.03$ mHz (fractional shift of 1.1×10^{-20}) with an uncertainty of 5 μHz (fractional uncertainty of 1.7×10^{-21}) and the relation between the SSS-based phase measurement uncertainty and the SQL of $(\Delta\phi)_{SSS}(V \neq 0) = \xi_W(V \neq 0) \times (\Delta\phi)_{SQL}$ with the Wineland parameter [18] $\xi_W^2(V \neq 0) = 0.027$. In contrast, we have $\xi_W^2(V = 0) = 0.0034$ in the absence of interatomic collisions. That is, the atom-atom interactions strongly degrade the metrological gain provided by spin squeezing.

IV. ULTRASTABLE LOCAL OSCILLATOR

The heart of an optical clock is an ultrastable laser source that is usually prestabilized to a well-engineered high-finesse optical resonator. This local oscillator primarily determines the short-term frequency stability of the optical clock. Stabilizing the local oscillator to a silicon resonator that is operated in cryogenic environment may reduce the laser's

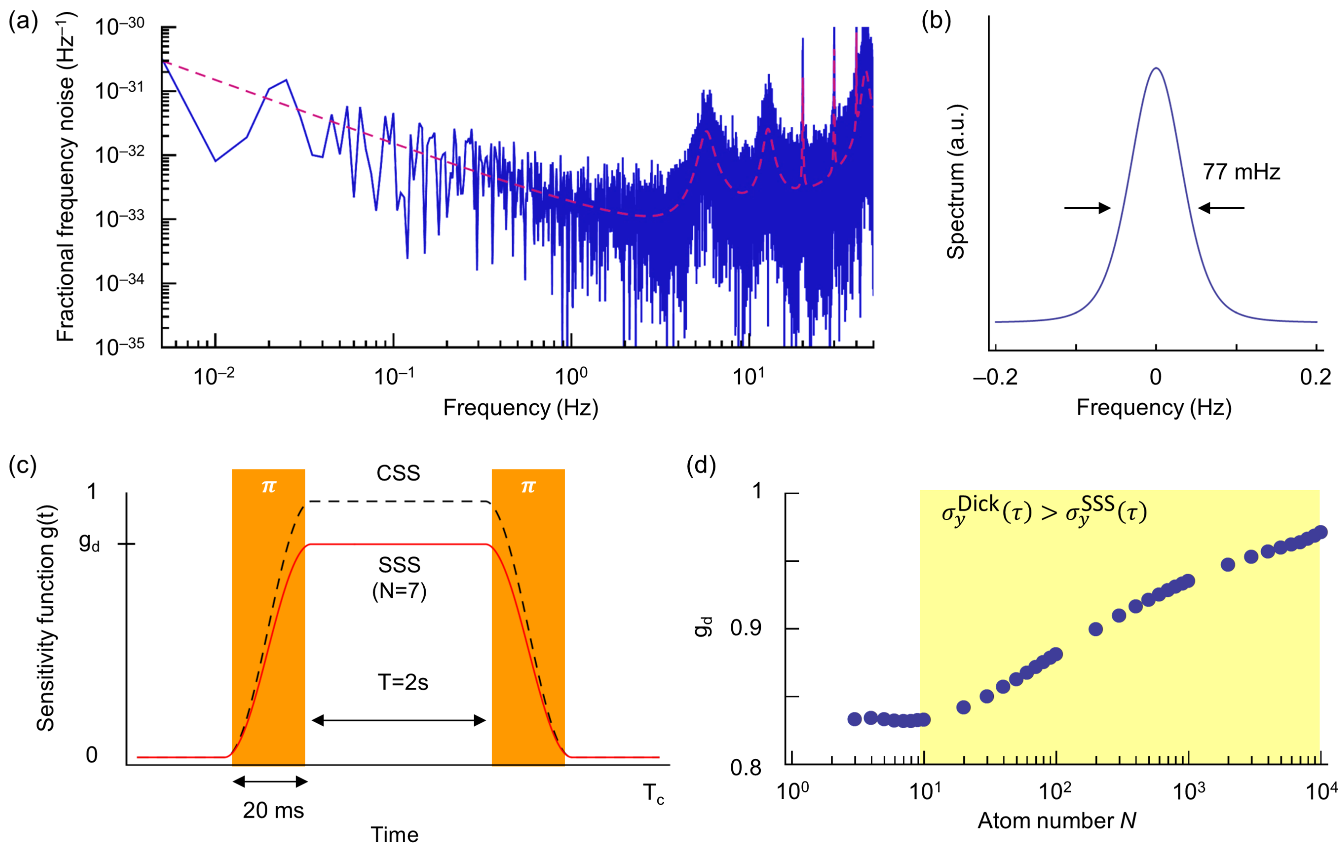

FIG. 5. Dick effect. (a) Frequency noise spectrum of the local oscillator. Solid line: numerical result. Dashed line: analytical model in [32]. (b) Power spectral density of the local oscillator. The clock laser has a spectral linewidth of 77 mHz. (c) Sensitivity function $g(t)$ for the Ramsey measurement based on CSS (dashed) and SSS (solid) with the atom number $N = 7$ in the absence of atom-atom interactions $V = 0$. The duration of light π pulses in Fig. 2(c) is set to be 20 ms. (d) Sensitivity g_d within the dark time vs atom number N. The shade denotes the regime of the Dick-effect-limited stability exceeding the SSS-based stability with $V = 0$, $\sigma_y^{\mathrm{Dick}}(\tau) > \sigma_y^{\mathrm{SSS}}(\tau)$.

spectral linewidth down to tens of mHz [52,53]. In addition, the resonator's thermal noise floor can be suppressed below 1×10^{-16}. We assume that the local oscillator has been locked to a cryogenic resonator with a frequency noise spectrum shown in Fig. 5(a). (This spectrum is numerically derived according to the analytical model in [32].) The resultant laser linewidth reaches $2\pi \times 77$ mHz [Fig. 5(b)], whose reciprocal gives the coherence time of the probe beam. Accordingly, we set the Ramsey measurement time as $T = 2$ s.

To evaluate the Dick effect based on this local oscillator, we compute the sensitivity function $g(t)$ of the atomic ensemble that is initially prepared in SSS in the absence of collisions $V = 0$ (see Appendix E). Since the spin squeezing suppresses the projection measurement noise, the sensitivity g_d within the dark period is lower than that of CSS ($g_d = 1$) as depicted in Fig. 5(c), resulting in a relatively weaker Dick effect. As the atom number N is increased, g_d goes up gradually toward unity [Fig. 5(d)].

Besides suppressing the probe beam noise, shortening the dead time in a clock cycle also effectively reduces the Dick limit. Using the cycle duration $T_c = 2.3$ s (i.e., 87% duty cycle) in [19], we derive the Dick-effect-limited clock stability as $\sigma_y^{\mathrm{Dick}}(\tau) = g_d \times 4.8 \times 10^{-17}/\sqrt{\tau}$. Indeed, the dead time may be further reduced even down to zero through alternatively interrogating multiensembles within a clock cycle [32,54].

We use $\sigma_y^{\mathrm{SQL/SSS}}(\tau)$ to denote the stability limit of the CSS/SSS-based Ramsey spectroscopy for one clock (ensemble) in the absence of atom-atom interactions,

$$\sigma_y^{\mathrm{SQL/SSS}}(\tau) = \frac{(\Delta\phi)_{\mathrm{SQL/SSS}}(V=0)}{2\pi\nu_0 T}\sqrt{\frac{T_c}{\tau}}, \tag{13}$$

with the frequency ν_0 of the clock $|g\rangle$-$|e\rangle$ transition. The numerical results illustrate that $\sigma_y^{\mathrm{Dick}}(\tau)$ exceeds $\sigma_y^{\mathrm{SQL}}(\tau)$ when $N > 33$ and $\sigma_y^{\mathrm{SSS}}(\tau)$ when $N > 9$, challenging a many-body optical clock beyond the Dick-effect limit. For the clock operation with $N = 5000$, we have $\sigma_y^{\mathrm{Dick}}(\tau) = 4.6 \times 10^{-17}/\sqrt{\tau}$, $\sigma_y^{\mathrm{SQL}}(\tau) = 3.3 \times 10^{-18}/\sqrt{\tau}$, and $\sigma_y^{\mathrm{SSS}}(\tau) = 2.0 \times 10^{-19}/\sqrt{\tau}$ with $V = 0$. That is, $\sigma_y^{\mathrm{Dick}}(\tau)$ is well above $\sigma_y^{\mathrm{SQL,SSS}}(\tau)$, limiting the frequency stability of individual optical clocks. The Dick limit can be overcome through the synchronous comparison [14,34].

V. CLOCK STABILITY

We perform the numerical simulation of the clock operation in the presence of collisional shifts $V \neq 0$ and evaluate the differential frequency stability between two optical clocks (i.e., two ensembles of atoms). Due to the finite amount of computer memory and computational time, we set $\bar{N} = 5000$, $\sigma_N = 50$, and $\bar{n} = 2$.

A. Simulation of clock operation

In the clock operation, the frequency locking point is set at the detuning $\Delta = \pi/2T$ between the probe beam and the clock $|g\rangle$ - $|e\rangle$ transition. Here, the fluctuations of lattice-induced light $\Delta\nu_{\rm LS}$ and BBR $\Delta\nu_{\rm BBR}$ shifts are omitted since their uncertainties are at the 10^{-21}–10^{-20} level. The detuning noise mainly comes from the frequency noise of the local oscillator $\Delta\nu_{\rm LO}(t)$ that is produced following the analytical model in [32].

For one Yb ensemble, the number of lattice-trapped atoms N varies over different clock cycles. Within the kth cycle, N is generated according to a Gaussian distribution with mean $\bar{N} = 5000$ and standard deviation $\sigma_N = 50$. The number of atoms on the mth site n_m obeys the Gaussian distribution under the condition that the average on-site atom number is equal to $\bar{n} = 2$. The atoms on the mth site are distributed over different radial motional (m_x, m_y) states according to the Fermi-Dirac statistics (see Appendix D).

For the kth clock cycle, we numerically compute the SSS-based Ramsey excitation of N atoms under the assumption that the light π pulses completely map the atoms from $|s\rangle$ into $|e\rangle$ and vice versa. We first compute the fractional Ramsey excitation of atoms $p = 1/2 + \langle\psi_f|\,(\hat{S}_z/N)\,|\psi_f\rangle$ with the ensemble wave function

$$|\psi_f\rangle = e^{-i\frac{\pi}{2}\hat{S}_x}\hat{\pi}\,e^{-i(\pi/2+\phi)\hat{J}_z}e^{-i2\pi\hat{V}T/h}\hat{\pi}\,|\psi_{\rm SSS}\rangle\,, \tag{14}$$

and $\hat{J}_z = \sum_{\mathbf{m}} \hat{j}^z_{\mathbf{m}}$. The extra phase difference ϕ accumulated between the laser and the clock transition over the dark period arises from the laser frequency noise $\Delta\nu_{\rm LO}(t)$. Then, the measured detuning Δ_k between the laser and the clock transition is evaluated by $\Delta_k = \Delta + (p - 1/2)/T + \delta_k$. Here, a small projection noise δ_k with the standard deviation of $(\Delta\phi)_{\rm SSS}/T$ [Fig. 4(d)] is artificially introduced to Δ_k. Finally, the detuning noise $\Delta\nu_{\rm LO}(t)$ is corrected according to Δ_k in the next clock cycle. Repeating the above process leads to the error signal in the corresponding acousto-optic modulator and the Allan deviation is evaluated accordingly.

B. Simulation results

The simulation results have been summarized in Fig. 6. Locking the local oscillator to the clock transition in one Yb ensemble overcomes the thermal noise floor of 4.6×10^{-17}, reaching the Dick-effect limit $\sigma_y^{\rm Dick}(\tau)$. The synchronous comparison between two Yb ensembles rejects the local oscillator noise. In the absence of atom-atom interactions, $V = 0$, the fractional stability of the differential frequency between two clocks with independent atoms (i.e., CSS) reaches $\sigma_y(\tau) = \sqrt{2}\sigma_y^{\rm SQL}(\tau) = 4.7 \times 10^{-18}/\sqrt{\tau}$, one order of magnitude lower than $\sigma_y^{\rm Dick}(\tau)$. Here, $\sqrt{2}$ comes from the fact that two ensembles are independent of each other. Employing the SSS further enhances the stability of the synchronous comparison, $\sigma_y(\tau) = \sqrt{2}\sigma_y^{\rm SSS}(\tau) = 2.8 \times 10^{-19}/\sqrt{\tau}$. In contrast, the atom-atom collisions, $V \neq 0$, induce the degradation of the differential frequency stability between two clocks, $\sigma_y(\tau) = 7.6 \times 10^{-19}/\sqrt{\tau}$ larger than $\sqrt{2}\sigma_y^{\rm SSS}(\tau)$. Nevertheless, the stability at the 10^{-19} level of 1 s averaging provides a powerful means for metrology and prime fundamental research. For example, the gravitational redshift across the 1-mm-width ultracold cloud on Earth's surface reaches -1.09×10^{-19}, which can be resolved through the SSS-based synchronous comparison over 50 s of averaging, less than 1/30th of that of [14].

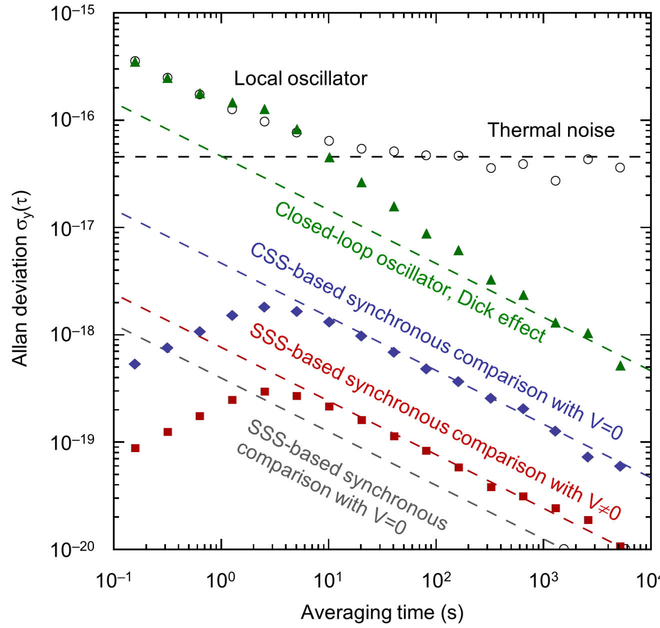

FIG. 6. Stabilities of the free-running local oscillator (circles), Dick-effect limit ($4.6 \times 10^{-17}/\sqrt{\tau}$, triangles), and synchronous comparisons based on CSS with $V = 0$ ($4.7 \times 10^{-18}/\sqrt{\tau}$, diamonds), SSS with $V = 0$ ($2.8 \times 10^{-19}/\sqrt{\tau}$), and SSS with $V \neq 0$ ($7.6 \times 10^{-19}/\sqrt{\tau}$, squares). For all curves, $\bar{N} = 5000$, $\sigma_N = 50$, $\bar{n} = 2$, $T = 2$ s, and $T_c = 2.3$ s.

VI. CONCLUSION

In summary, we have theoretically studied the performance of spin-squeezing-based shallow-lattice Yb optical clocks. For single clocks, the Dick effect far outweighs the advantage of many-body entanglement and primarily limits the clock precision, thereby necessitating significant improvements in shortening the dead time and lowering the clock laser phase noise. In contrast, the differential frequency measurement effectively rejects the Dick noise, leading to a clock stability beyond the Dick limit. However, the atom-atom interactions degrade the metrological gain provided by spin squeezing, weakening its advantage in clock performance. Our numerical simulation shows that the potential stability of spin-squeezing-based synchronous comparison may access the 10^{-19} level at the averaging time of 1 s. Lowering the atomic temperature and reducing the density of atoms may further enhance the differential frequency stability.

Besides using spin squeezing to suppress the variance of the phase measurement, an alternative way to enhance the phase sensitivity is to directly amplify the small phase shift itself through a time-reversal interaction protocol [55,56]. This protocol employs a controlled sign change in the many-body spin Hamiltonian and has achieved a metrological gain of 11.8 dB in experiment [55]. Additionally, the dependence of the phase sensitivity on the atom number shows a Heisenberg scaling (b/N) that is at a fixed distance of $b = 12.6$ dB from the Heisenberg limit.

ACKNOWLEDGMENTS

D.Y. acknowledges funding provided by the National Time Service Center, China (E239SC1101). J.C. is supported by the Innovation Program for Quantum Science and Technology (2021ZD0303200). T.S. is grateful for support from the China Postdoctoral Science Foundation (BX2021020).

APPENDIX A: SPIN SQUEEZING

The inset of Fig. 1 illustrates the general procedure for creating the SSS. Initially, all atoms are prepared in the $|g\rangle$ state. A rf $\frac{\pi}{2}$ pulse is used to resonantly drive the $|g\rangle$ - $|s\rangle$ transition in atom, resulting in the CSS $|\psi_{\text{CSS}}\rangle$ [see Eq. (1)]. Then, the one-axis twisting interaction (duration of α) and the rotation of the system around the y axis by an angle ($\beta - \frac{\pi}{2}$) are performed on the atomic cloud sequentially, leading to the SSS $|\psi_{\text{SSS}}\rangle$ [see Eq. (2)]. The angular momentum operators $\hat{S}_{x,y,z}$ in Eqs. (1) and(2) are defined as

$$\hat{S}_x = \frac{1}{2}\sum_{\mathbf{m}}\left[\hat{\sigma}_{sg}^{(\mathbf{m})} + \hat{\sigma}_{gs}^{(\mathbf{m})}\right], \tag{A1a}$$

$$\hat{S}_y = -\frac{i}{2}\sum_{\mathbf{m}}\left[\hat{\sigma}_{sg}^{(\mathbf{m})} - \hat{\sigma}_{gs}^{(\mathbf{m})}\right], \tag{A1b}$$

$$\hat{S}_z = \frac{1}{2}\sum_{\mathbf{m}}\left[\hat{\sigma}_{ss}^{(\mathbf{m})} - \hat{\sigma}_{gg}^{(\mathbf{m})}\right], \tag{A1c}$$

and the operator, for example, $\hat{\sigma}_{sg}^{(\mathbf{m})} = (|s\rangle\langle g|)_{\mathbf{m}}$, is associated with the atom in the motional $\mathbf{m}$ state (see below). According to [18], the optimal pair of angles (α, β) minimizes the phase uncertainty in Ramsey spectroscopy,

$$(\Delta\phi)_{\text{SSS}} = \min\left[\frac{\Delta S_x(\phi)}{S_z(\phi)}\right]_{\phi=\pm\pi/2}, \tag{A2}$$

with the expectation $O(\phi) = \langle\psi_f(\phi)|\,\hat{O}\,|\psi_f(\phi)\rangle$ and uncertainty $\Delta O(\phi) = \sqrt{\langle\psi_f(\phi)|\,\hat{O}^2\,|\psi_f(\phi)\rangle - O^2(\phi)}$ of an operator $\hat{O}$ in $|\psi_f(\phi)\rangle$ [see Eq. (4)] and the phase difference ϕ between two pulses in the Ramsey measurement. For independent atoms, we have $|\psi_f(\phi)\rangle = e^{-i\frac{\pi}{2}\hat{S}_x}e^{-i\phi\hat{S}_z}|\psi_{\text{CSS}}\rangle$, under which the phase uncertainty at $\phi = \pm\pi/2$ corresponds to the SQL of the phase measurement, $(\Delta\phi)_{\text{SQL}} = N^{-0.5}$.

Figure 7 displays the dependence of $S_z(\phi)$ and $\Delta S_z(\phi)$ on ϕ. At the frequency locking point of the local oscillator, $\phi = \pm\pi/2$, the population inversion S_z is equal to 0.0 (i.e., the fractional excitation of 0.5) for both CSS and SSS. In contrast, the excitation uncertainty ΔS_z under the CSS is much higher than that of SSS (i.e., spin squeezing).

We numerically compute the dependence of $(\Delta\phi)_{\text{CSS}}$ on the atom number N (Fig. 1) and find the scaling $(\Delta\phi)_{\text{SSS}} \sim N^{-0.83}$. The Wineland parameter is defined as $\xi_{\text{W}} = (\Delta\phi)_{\text{SSS}}/(\Delta\phi)_{\text{SQL}}$.

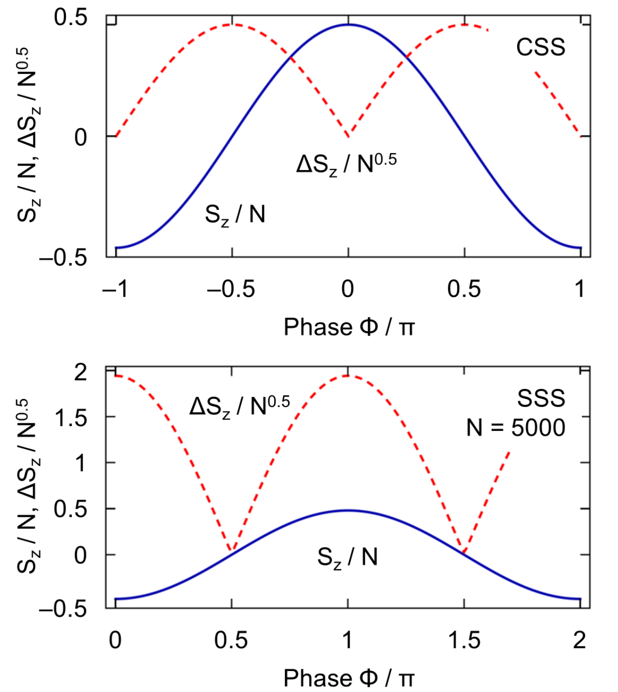

FIG. 7. Dependence of the expectation $S_z(\phi)$ and uncertainty $\Delta S_z(\phi)$ on ϕ for Ramsey detection using the CSS (upper) and SSS (lower). The atom number is $N = 5000$.

APPENDIX B: WANNIER-STARK STATES

We consider the localization of atoms in the optical lattice. The Hamiltonian that governs the external motion of atoms in the axial direction is written as

$$\hat{H}_{\text{ext}} = \hat{H}_{\text{ext}}^{(0)} + Mg\hat{z}, \tag{B1}$$

with the acceleration of the Earth's gravity g. Here, the Hamiltonian

$$\hat{H}_{\text{ext}}^{(0)} = \frac{\hat{p}_z^2}{2M} + \frac{U_0}{2}(1 - \cos 2k_L\hat{z}), \tag{B2}$$

describes the atom moving in the periodic optical potential with the momentum of atom $\hat{p}_z$. Before deriving the eigenvalues and eigenstates of $\hat{H}_{\text{ext}}$, let us first focus on the following eigenvalue equation

$$\hat{H}_{\text{ext}}^{(0)}\psi_{n,q}(z) = \hbar\omega_{n,q}^{(0)}\psi_{n,q}(z), \tag{B3}$$

with the band index n and the momentum q. According to Bloch's theorem, $\psi_{n,q}(z)$ takes the form

$$\psi_{n,q}(z) = \sum_{\mu} c_{n,\mu,q}e^{i(q+2\mu k_L)z}, \tag{B4}$$

where $c_{n,\mu,q}$ and $\omega_{n,q}^{(0)}$ can be derived from

$$\hbar\omega_{n,q}c_{n,\mu,q} = \left[\frac{(q+2\mu k_L)^2}{2} + \frac{U_0}{2}\right]c_{n,\mu,q} - \frac{U_0}{4}(c_{n,\mu-1,q} + c_{n,\mu+1,q}). \tag{B5}$$

We restrict ourselves to $n = 0$, i.e., $\psi_q(z) = \psi_{n,q}(z)$ and $\omega_q^{(0)} = \omega_{n,q}^{(0)}$, since the atoms are usually initialized in the ground band in the clock operation. One may use the Bloch

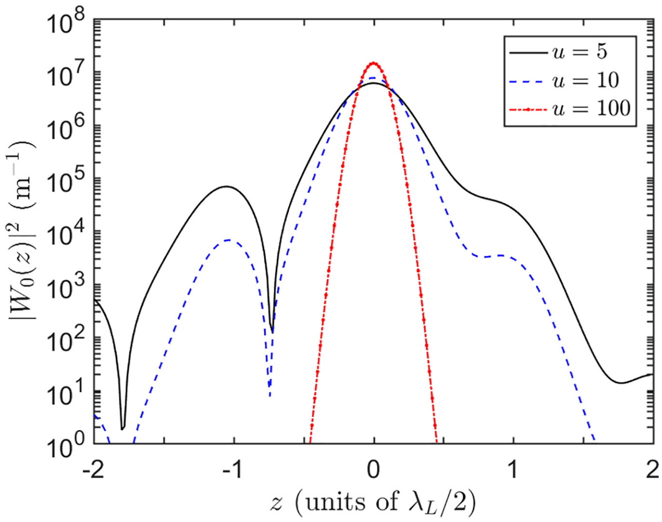

FIG. 8. Wannier-Stark states of Yb atoms moving in the optical lattice with different potentials $u = U_0/E_R$.

states $\psi_q(z)$ to construct the eigenstate of an atom localized on the mth lattice site,

$$W_m(z) = \sum_q b_{m,q}\psi_q(z), \tag{B6}$$

which is the solution to the eigenvalue equation

$$\hat{H}_{\rm ext}W_m(z) = \hbar\omega_m W_m(z). \tag{B7}$$

As illustrated in Ref. [57], ω_m takes the form

$$\omega_m = \omega_0 + m\Delta, \tag{B8}$$

with the mean frequency of Bloch states $\omega_0 = \frac{1}{N}\sum_q \omega_q^{(0)}$ and the energy separation between adjacent lattice sites $\Delta = \frac{Mg\lambda_L}{2\hbar}$. $b_{m,q}$ is derived as

$$b_{m,q} = \frac{1}{\sqrt{N}}\exp\left[-\frac{i\hbar}{Mg}(q\omega_m - \tilde{\omega}_q)\right], \tag{B9}$$

with $\frac{\partial\tilde{\omega}_q}{\partial q} = \omega_q^{(0)}$ and $\tilde{\omega}_0 = 0$. The $W_m(z)$ states are usually referred to as the Wannier-Stark states. As shown in Fig. 8, for a lattice potential as shallow as $U_0 = 5E_R$ the population of an atom in nearest-neighbor sites is fifty times smaller than the main population peak.

APPENDIX C: LIGHT SHIFTS

Although the lattice-induced light shift $\Delta\nu_{\rm LS}$ has already been formulated in [58–60], here we rederive $\Delta\nu_{\rm LS}$ and find a different expression caused by the inhomogeneous distribution of the lattice intensity in the radial direction. The atoms move in the optical lattice formed by the interference of two Gaussian beams (waist w_0) of the same frequency ν_L (wavelength λ_L and wave number k_L) and amplitude traveling in opposite directions (in the z axis). To the fourth-order Stark shift, the optical potential experienced by an atom in $|\mu = e, g\rangle$ is written as [58–60]

$$\hat{U}_\mu(\mathbf{r}) \approx -\left[\alpha_\mu^{E1}(\nu_L) - \alpha_\mu^{dqm}(\nu_L)\sin^2(k_L\hat{z})\right]Ie^{-\frac{2(x^2+y^2)}{w_0^2}} - \beta_\mu(\nu_L)\cos^4(k_L\hat{z})I^2e^{-\frac{4(x^2+y^2)}{w_0^2}}, \tag{C1}$$

where α_μ^{dqm} denotes the difference between the electric-dipole α_μ^{E1} and the sum α_μ^{qm} of magnetic-dipole and electric-quadrupole dynamic polarizabilities, β_μ accounts for the electric-dipole dynamic hyperpolarizability, and I is the intensity of single traveling beam. The magic wavelength $\lambda_{\rm magic}$ of the optical lattice is defined according to $\alpha_e^{E1}(\nu_{\rm magic}) = \alpha_g^{E1}(\nu_{\rm magic}) \equiv \alpha_0^{E1}$ with $\nu_{\rm magic} = c/\lambda_{\rm magic}$ (with the speed of light in free space c) [41]. In the practical clock operation, the lattice laser frequency ν_L is detuned from $\nu_{\rm magic}$ by a small amount $\delta_L = \nu_L - \nu_{\rm magic}$.

The energy of an atom moving in $\hat{U}_\mu(\mathbf{r})$ is quantized. In the axial direction, the atoms are localized on individual lattice sites (see below). One may expand $\sin^2(k_L\hat{z})$ and $\cos^4(k_L\hat{z})$ in Eq. (C1) up to harmonic ($\propto \hat{z}^2$) and anharmonic ($\propto \hat{z}^4$) terms. We apply the approximation of the quantum harmonic oscillator,

$$|n\rangle = (\xi\sqrt{\pi}2^n n!)^{-1/2}\mathscr{H}_n(z/\xi)e^{-z^2/2\xi^2}, \tag{C2}$$

with $\xi = \sqrt{\frac{\hbar}{M\Omega_z}}$, the reduced Planck constant $\hbar$, the mass of an atom M, the characteristic frequency $\Omega_z = 2\sqrt{U_0E_R}/\hbar$ in the axis direction, the lattice potential $U_0 = \alpha_0^{E1}I$, the photon-recoil energy $E_R = \frac{h^2}{2M\lambda_L^2}$, and the Hermite polynomials $\mathscr{H}_n(z/\xi)$. The light shift of the clock transition $\Delta\nu_{\rm LS}$ is computed by

$$h\Delta\nu_{\rm LS} = \int \rho(x,y)\,\langle n|\,[\hat{U}_e(\mathbf{r}) - \hat{U}_g(\mathbf{r})]\,|n\rangle\,dx\,dy, \tag{C3}$$

with the Planck constant h and the thermal distribution

$$\rho(x,y) = \frac{M\Omega_r^2}{2\pi k_BT_r}e^{-\frac{M\Omega_r^2}{2k_BT_r}(x^2+y^2)}, \tag{C4}$$

of atoms in the radial direction [$\int\rho(x,y)dx\,dy = 1$], the radial temperature T_r, the Boltzmann constant k_B, and the radial oscillation frequency $\Omega_r = \sqrt{\frac{4U_0}{Mw_0^2}}$. Equation (C3) indicates that the radial motion of atoms is treated classically.

After some algebra, we arrive at [8]

$$\begin{aligned} h\Delta\nu_{\rm LS} = {} & \sqrt{p}\left(\frac{\partial\Delta\tilde{\alpha}^{E1}}{\partial\nu}\delta_L - \Delta\tilde{\alpha}^{qm}\right)\left(n+\frac{1}{2}\right)u^{1/2} \\ & -\left[p\frac{\partial\Delta\tilde{\alpha}^{E1}}{\partial\nu}\delta_L + \frac{3q}{2p}\Delta\tilde{\beta}\left(n^2+n+\frac{1}{2}\right)\right]u \\ & +\frac{2q}{\sqrt{p}}\Delta\tilde{\beta}\left(n+\frac{1}{2}\right)u^{3/2} - q\Delta\tilde{\beta}u^2, \end{aligned} \tag{C5}$$

with $\Delta\tilde{\alpha}^{E1} = (E_R/\alpha_0^{E1})(\alpha_e^{E1} - \alpha_g^{E1})$, $\Delta\tilde{\alpha}^{qm} = (E_R/\alpha_0^{E1})(\alpha_e^{qm} - \alpha_g^{qm})$, $\Delta\tilde{\beta} = (E_R/\alpha_0^{E1})^2(\beta_e - \beta_g)$, $p = (1 + k_BT_r/U_0)^{-1}$, $q = (1 + 2k_BT_r/U_0)^{-1}$, and $u = U_0/E_R$. In the limit $k_BT_r \ll U_0$, one has $p \approx q \approx 1$ and Eq. (C5) is reduced to the one in [58–60].

The light shift coefficients for Sr and Yb have been listed in Table I. In the clock operation, the atoms are usually prepared in the axial ground vibrational state $n = 0$. The radial temperature T_r has a typical value of 0.2 μK and the condition $k_BT_r \ll U_0$ is not satisfied.

TABLE I. Electric-dipole (α_0^{E1}), difference of multipolar ($\Delta\tilde{\alpha}^{qm}$) and hyper ($\Delta\tilde{\beta}$) polarizabilities for Sr and Yb at the magic wavelength $\lambda_{\rm magic}$.

	Sr [8]	Yb [9,60]
$\lambda_{\rm magic}$ (nm)	813.43	759.36
$\frac{\alpha_0^{E1}}{h}$ $(\frac{\rm kHz}{\rm kW/cm^2})$	54.1	40.5
$\frac{1}{h}\frac{\partial\Delta\tilde{\alpha}^{E1}}{\partial\nu}$ $(\frac{\mu\rm Hz}{\rm MHz})$	17.35	25.74
$\frac{\Delta\tilde{\alpha}^{qm}}{h}$ (μHz)	−962	−1027
$\frac{\Delta\tilde{\beta}}{h}$ (μHz)	−0.461	−1.194

APPENDIX D: COLLISIONS OF SPIN-POLARIZED ATOMS

We employ the spin model approximation to investigate the collisional shifts in shallow-lattice optical clocks [48]. Let us assume that the light π pulses can completely map the $|s\rangle$-populated atoms into $|e\rangle$ and vice versa [Fig. 2(b)]. Thus, any quantum operations carried out between $|g\rangle$ and $|s\rangle$ are equivalent to performing the same operations on the two-level system composed of $|g\rangle$ and $|e\rangle$. We use $\mathbf{m}=(m_x, m_y, m)$ to denote the motional state that is populated by one fermionic atom. This atom undergoes the radial vibration with the harmonic oscillator eigenmodes $\phi_{m_x}(x)$ and $\phi_{m_y}(y)$ and is localized on the mth lattice site with the corresponding Wannier–Stark state $W_m(z)$. The operator $\hat{\mathbf{j}}_{\mathbf{m}}=\hat{j}^x_{\mathbf{m}}\mathbf{e}_x+\hat{j}^y_{\mathbf{m}}\mathbf{e}_y+\hat{j}^z_{\mathbf{m}}\mathbf{e}_z$ associated with the $\mathbf{m}$ atom is given by

$$\hat{j}^x_{\mathbf{m}}=\left[\hat{\sigma}^{(\mathbf{m})}_{eg}+\hat{\sigma}^{(\mathbf{m})}_{ge}\right]/2, \tag{D1a}$$

$$\hat{j}^y_{\mathbf{m}}=-i\left[\hat{\sigma}^{(\mathbf{m})}_{eg}-\hat{\sigma}^{(\mathbf{m})}_{ge}\right]/2, \tag{D1b}$$

$$\hat{j}^z_{\mathbf{m}}=\left[\hat{\sigma}^{(\mathbf{m})}_{ee}-\hat{\sigma}^{(\mathbf{m})}_{gg}\right]/2, \tag{D1c}$$

with $\hat{\sigma}^{(\mathbf{m})}_{uv}=(|u\rangle\langle v|)_{\mathbf{m}}$ $(u,v=e,g)$.

The atom-atom interaction Hamiltonian including s- and p-wave contributions takes the form [15]

$$\begin{aligned}\hat{V}=\sum_{\mathbf{m}\neq\mathbf{m}'}&\Big[\big(B^{eg}_{\mathbf{m},\mathbf{m}'}-A_{\mathbf{m},\mathbf{m}'}\big)\hat{\mathbf{j}}_{\mathbf{m}}\cdot\hat{\mathbf{j}}_{\mathbf{m}'}\\&+\big(B^{ee}_{\mathbf{m},\mathbf{m}'}+B^{gg}_{\mathbf{m},\mathbf{m}'}-B^{eg}_{\mathbf{m},\mathbf{m}'}\big)\hat{j}^z_{\mathbf{m}}\hat{j}^z_{\mathbf{m}'}\\&+\big(B^{ee}_{\mathbf{m},\mathbf{m}'}-B^{gg}_{\mathbf{m},\mathbf{m}'}\big)\big(\hat{j}^z_{\mathbf{m}}\hat{n}_{\mathbf{m}'}+\hat{n}_{\mathbf{m}}\hat{j}^z_{\mathbf{m}'}\big)/2\Big],\end{aligned} \tag{D2}$$

where the interaction parameters are defined as

$$A_{\mathbf{m},\mathbf{m}'}=\frac{4\pi\hbar a^-_{eg}}{M}q_{m_x,m'_x}q_{m_y,m'_y}o_{m,m'}, \tag{D3a}$$

$$B^{uv}_{\mathbf{m},\mathbf{m}'}=\frac{3\pi\hbar^2b^3_{uv}}{2M}(p_{m_x,m'_x}q_{m_y,m'_y}+q_{m_x,m'_x}p_{m_y,m'_y})o_{m,m'}, \tag{D3b}$$

with the s-wave scattering length a^-_{eg}, the p-wave scattering volumes b^3_{uv} $(u,v=e,g)$, and the overlap integrals, for example,

$$p_{m_x,m'_x}=\int\left|\phi_{m_x}(x)\frac{\partial}{\partial x}\phi_{m'_x}(x)-\phi_{m'_x}(x)\frac{\partial}{\partial x}\phi_{m_x}(x)\right|^2dx, \tag{D4a}$$

$$q_{m_x,m'_x}=\int|\phi_{m_x}(x)\phi_{m'_x}(x)|^2dx, \tag{D4b}$$

$$o_{m,m'}=\int|W_m(z)W_{m'}(z)|^2dz. \tag{D4c}$$

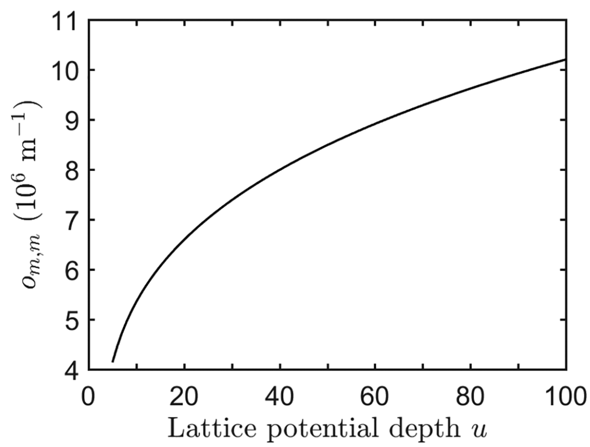

FIG. 9. Overlap integral $o_{m,m}$ for Yb as a function of the lattice potential depth u.

Figure 9 illustrates that $o_{m,m}$ decreases as the lattice potential u is reduced. When $u\geqslant5$, $o_{m,m}$ is over 60 times larger than $o_{m,m'}$ with $|m'-m|=1$.

In the absence of excitation inhomogeneity, the Dicke states $\{|M\rangle\equiv|J,M\rangle, M=-J,\ldots,J\}$ with $J=N/2$ can be used to span the Hilbert space if all atoms are initialized in $|g\rangle$. As a result, s-wave collisions, which mainly occur between atoms in different lattice sites $(m\neq m')$, are substantially suppressed. Indeed, the recent experiment has verified the dominant role of p-wave collisions between on-site atoms in fermionic Yb lattice clocks [49].

We focus on the influence of atom-atom interactions on the SSS-based Ramsey spectroscopy [Fig. 2(c)]. Collisions during the short light π pulses can be ignored. The interaction $\hat{V}$ governs the dynamics of atoms within the dark period T. It is easy to derive the following transition matrix elements:

$$\langle M'|\,\hat{j}^{\pm}_{\mathbf{m}}\,|M\rangle=\frac{\sqrt{(J\pm M+1)(J\mp M)}}{2J}\delta_{M',M\pm1}, \tag{D5a}$$

$$\langle M'|\,\hat{j}^{z}_{\mathbf{m}}\,|M\rangle=\frac{M}{2J}\delta_{M',M}. \tag{D5b}$$

Thus, $\hat{V}$ is diagonal in the Dicke-state basis and each $|M\rangle$ acquires an extra phase shift after the free evolution time. All these different phases eventually lead to the clock frequency shift.

Let us consider the distribution of atoms in the optical lattice potential. In each clock cycle, the ultracold atomic cloud with the Gaussian distribution $\sim e^{-4(z_m-z_c)^2/L_z^2}$ in the axial direction is loaded into the lattice [51] and all atoms are initially prepared in the ground $(n=0)$ band. Here, z_c corresponds to the lattice center and L_z denotes the axial width at half maximum of the atomic cloud. One may numerically generate the number of atoms n_m in the mth site accordingly in the simulation (Fig. 10). The conservation of atom number demands $N=\sum_m n_m$ and the average of the on-site atom number is given by $\bar{n}=N\lambda_L/2L_z$. Additionally, in the radial direction, the atoms on a lattice site follow the Fermi-Dirac distribution

$$f_{m_r}=\frac{m_r+1}{e^{[(m_r+1)\hbar\Omega_r-k_BT_F]/k_BT_r}+1}, \tag{D6}$$

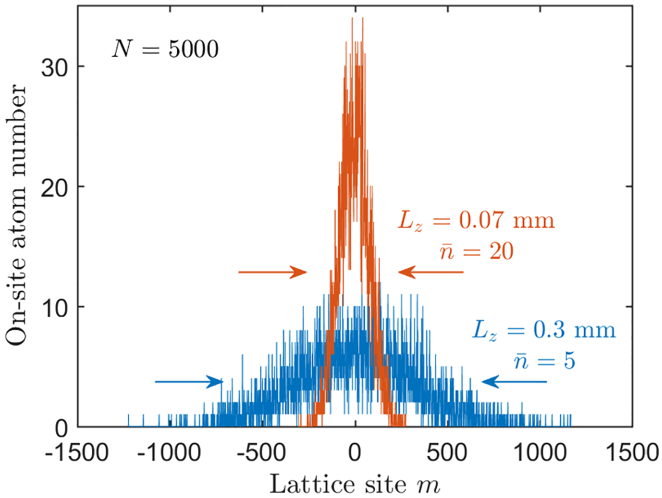

FIG. 10. Distribution of lattice-trapped atoms in the axis direction.

with the radial quantum number m_r and the Fermi temperature T_F. For each populated lattice site $n_m \geqslant 1$, one may numerically generate the indices m_r according to Eq. (D6) and then randomly select (m_x, m_y) under the condition of $m_r = m_x + m_y$. Finally, we obtain a set of populated motional **m** states. Substituting $a_{eg}^- = -25a_0$ (a_0 the Bohr radius), $b_{eg} = -74a_0$, $b_{ee}^3 = 0.1b_{eg}^3$, and $b_{gg} \approx 0$ for Yb [49] and the typical value $T_F \sim 100$ nK, one may compute the time evolution of wave function of atoms within the dark time and further study the effects of atom-atom interactions on the SSS-based Ramsey spectroscopy, including the collisional shift and the degradation of the spin squeezing (Fig. 4).

APPENDIX E: DICK EFFECT

The down-conversion of the local oscillator's intrinsic frequency noise degrades the short-term frequency stability of an atomic clock, known as the Dick effect [29]. Thus far, the Dick effect for independent atoms has been well formulated, but few studies have been focused on the Dick effect associated with the SSSs. Here, we study the Dick effect in a spin-squeezing-based optical clock under Ramsey interrogation.

Let us first derive the sensitivity function $g(t)$ of the system to the phase step φ of the probe beam. Each clock cycle (duration of T_c) begins with the preparation of all atoms in $|g\rangle$. The one-axis twisting method in Appendix A is implemented to create the SSS of atoms. Subsequently, the system evolves according to the Schrodinger equation

$$i\hbar\frac{d}{d\tau}|\psi(\tau)\rangle = \hat{H}_{\text{Ramsey}}|\psi(\tau)\rangle, \tag{E1}$$

with the light-atom interaction Hamiltonian

$$\hat{H}_{\text{Ramsey}}/\hbar = \sum_{\mathbf{m}}\left[-\Delta\hat{\sigma}_{ee}^{(\mathbf{m})} + \frac{\Omega(\tau)}{2}\hat{\sigma}_{se}^{(\mathbf{m})}e^{-i\varphi(\tau)} + \frac{\Omega(\tau)}{2}\hat{\sigma}_{es}^{(\mathbf{m})}e^{i\varphi(\tau)}\right], \tag{E2}$$

the detuning Δ of the probe beam relative to the $|s\rangle$-$|e\rangle$ transition, the Rabi frequency

$$\Omega(\tau) = \begin{cases}\pi/\tau_\pi, & 0 \leqslant \tau \leqslant \tau_\pi,\\ 0, & \tau_\pi < \tau < \tau_\pi +, T\\ \pi/\tau_\pi, & \tau_\pi + T \leqslant \tau \leqslant 2\tau_\pi + T,\end{cases} \tag{E3}$$

a small phase step $\varphi(t)$ occurring at the time t,

$$\varphi(\tau) = \begin{cases}0, & 0 \leqslant \tau < t,\\ \varphi, & t \leqslant \tau,\end{cases} \tag{E4}$$

and the initial condition $|\psi(0)\rangle = |\psi_{\text{SSS}}\rangle$. Actually, $\hat{H}_{\text{Ramsey}}$ denotes that a π pulse maps the $|s\rangle$-populated atoms into $|e\rangle$ and a second π pulse maps the $|e\rangle$-populated atoms back into $|s\rangle$. The system evolves freely between two pulses. The detuning is usually set at $\Delta = \pi/2T$ for the clock operation.

Finally, a second rf $\frac{\pi}{2}$ pulse resonantly drives the atoms to

$$|\psi_f\rangle = e^{-i\pi\hat{S}_x/2}|\psi(2\tau_\pi + T)\rangle, \tag{E5}$$

on which the projection measurement is performed. The sensitivity function $g(t)$ is given by [29]

$$g(t) = -\frac{2}{N}\frac{\partial}{\partial\varphi}\langle\psi_f|\hat{S}_z|\psi_f\rangle. \tag{E6}$$

Accordingly, the Dick-effect-limited Allan deviation of the locked local oscillator is computed by

$$\left[\sigma_y^{\text{Dick}}(\tau)\right]^2 = \frac{1}{\tau}\sum_{n=1}^{\infty}|g_n/g_0|^2 S_y^f(n/T_c), \tag{E7}$$

with the parameters

$$g_n = \frac{1}{T}\int_0^{T_c} g(t)e^{-i\frac{2\pi nt}{T_c}}\,dt, \tag{E8}$$

and the one-sided power spectral density $S_y^f(n/T_c)$ of relative frequency fluctuations of the free running local oscillator at frequencies n/T_c. As illustrated in Fig. 5(c), $g(t)$ grows strongly from zero to a value $g_d < 1$ within the first light π pulse, stays at g_d during the dark period, and rapidly goes down to zero when the second light π pulse is launched.

Thus far, no approximation has been made. However, it is challenging to solve Eqs. (E1) and (E2) for a large number of atoms due to the extremely expanded space dimension 3^N. One may use the approximation

$$g(t) \approx (g_d/2)(1 - \cos\pi t/\tau_\pi), \tag{E9}$$

during the first light π pulse and

$$g(t) \approx (g_d/2)[1 + \cos\pi(t - \tau_\pi - T)/\tau_\pi], \tag{E10}$$

within the second light π pulse duration to estimate $\sigma_y^{\text{Dick}}(\tau)$. Additionally, in the limit $T \gg (\tau_\pi/2)$, two light π pulses nearly transfer all atoms between $|s\rangle$ and $|e\rangle$. Thus, one may approximately evaluate g_d using the two-level model,

$$g_d \approx \left|\frac{\partial}{\partial\varphi}\langle\psi_{\text{SSS}}|e^{i\pi\hat{S}_x/2}(\hat{S}_z/N)e^{-i\pi\hat{S}_x/2}|\psi_{\text{SSS}}\rangle\right|. \tag{E11}$$

Using Eqs. (E9)–(E11), the Dick-effect-limited Allan deviation can be evaluated for a large ensemble of atoms.

[1] A. D. Ludlow, M. M. Boyd, J. Ye, E. Peik, and P. O. Schmidt, Rev. Mod. Phys. **87**, 637 (2015).

[2] B. J. Bloom, T. L. Nicholson, J. R. Williams, S. L. Campbell, M. Bishof, X. Zhang, W. Zhang, S. L. Bromley, and J. Ye, Nature (London) **506**, 71 (2014).

[3] I. Ushijima, M. Takamoto, M. Das, T. Ohkubo, and H. Katori, Nat. Photon **9**, 185 (2015).

[4] X. Zhang, M. Bishof, S. L. Bromley, C. V. Kraus, M. S. Safronova, P. Zoller, A. M. Rey, and J. Ye, Science **345**, 1467 (2014).

[5] F. Scazza, C. Hofrichter, M. Höfer, P. C. De Groot, I. Bloch, and S. Fölling, Nat. Phys. **10**, 779 (2014).

[6] N. Nemitz, T. Ohkubo, M. Takamoto, I. Ushijima, M. Das, N. Ohmae, and H. Katori, Nat. Photon **10**, 258 (2016).

[7] A. Derevianko and M. Pospelov, Nat. Phys. **10**, 933 (2014).

[8] I. Ushijima, M. Takamoto, and H. Katori, Phys. Rev. Lett. **121**, 263202 (2018).

[9] N. Nemitz, A. A. Jørgensen, R. Yanagimoto, F. Bregolin, and H. Katori, Phys. Rev. A **99**, 033424 (2019).

[10] K. Kim, A. Aeppli, T. Bothwell, and J. Ye, Phys. Rev. Lett. **130**, 113203 (2023).

[11] R. J. Fasano, Y. J. Chen, W. F. McGrew, W. J. Brand, R. W. Fox, and A. D. Ludlow, Phys. Rev. Appl. **15**, 044016 (2021).

[12] S. Dörscher, R. Schwarz, A. Al-Masoudi, S. Falke, U. Sterr, and C. Lisdat, Phys. Rev. A **97**, 063419 (2018).

[13] X. Zheng, J. Dolde, V. Lochab, B. N. Merriman, H. Li, and S. Kolkowitz, Nature (London) **602**, 425 (2022).

[14] T. Bothwell, C. J. Kennedy, A. Aeppli, D. Kedar, J. M. Robinson, E. Oelker, A. Staron, and J. Ye, Nature (London) **602**, 420 (2022).

[15] A. Aeppli, A. Chu, T. Bothwell, C. J. Kennedy, D. Kedar, P. He, A. M. Rey, and J. Ye, Sci. Adv. **8**, eadc9242 (2022).

[16] W. M. Itano, J. C. Bergquist, J. J. Bollinger, J. M. Gilligan, D. J. Heinzen, F. L. Moore, M. G. Raizen, and D. J. Wineland, Phys. Rev. A **47**, 3554 (1993).

[17] G. Santarelli, Ph. Laurent, P. Lemonde, A. Clairon, A. G. Mann, S. Chang, A. N. Luiten, and C. Salomon, Phys. Rev. Lett. **82**, 4619 (1999).

[18] D. J. Wineland, J. J. Bollinger, W. M. Itano, and D. J. Heinzen, Phys. Rev. A **50**, 67 (1994).

[19] E. Pedrozo-Peñafiel, S. Colombo, C. Shu, A. F. Adiyatullin, Z. Li, E. Mendez, B. Braverman, A. Kawasaki, D. Akamatsu, Y. Xiao, and V. Vuletić, Nature (London) **588**, 414 (2020).

[20] W. J. Eckner, N. D. Oppong, A. Cao, A. W. Young, W. R. Milner, J. M. Robinson, J. Ye, and A. M. Kaufman, Nature (London) **621**, 734 (2023).

[21] J. Franke, S. R. Muleady, R. Kaubruegger, F. Kranzl, R. Blatt, A. M. Rey, M. K. Joshi, and C. F. Roos, Nature (London) **621**, 740 (2023).

[22] J. M. Robinson, M. Miklos, Y. M. Tso, C. J. Kennedy, T. Bothwell, D. Kedar, J. K. Thompson, and J. Ye, Nat. Phys. **20**, 208 (2024).

[23] J. Chen and D. Yu, Sci. Bull. **69**, 1359 (2024).

[24] J. J. Bollinger, W. M. Itano, D. J. Wineland, and D. J. Heinzen, Phys. Rev. A **54**, R4649 (1996).

[25] B. C. Nichol, R. Srinivas, D. P. Nadlinger, P. Drmota, D. Main, G. Araneda, C. J. Ballance, and D. M. Lucas, Nature (London) **609**, 689 (2022).

[26] D. Leibfried, E. Knill, S. Seidelin, J. Britton, R. B. Blakestad, J. Chiaverini, D. B. Hume, W. M. Itano, J. D. Jost, C. Langer, R. Ozeri, R. Reichle, and D. J. Wineland, Nature (London) **438**, 639 (2005).

[27] T. Monz, P. Schindler, J. T. Barreiro, M. Chwalla, D. Nigg, W. A. Coish, M. Harlander, W. Hänsel, M. Hennrich, and R. Blatt, Phys. Rev. Lett. **106**, 130506 (2011).

[28] A. Omran, H. Levine, A. Keesling, G. Semeghini, T. T. Wang, S. Ebadi, H. Bernien, A. S. Zibrov, H. Pichler, S. Choi, J. Cui, M. Rossignolo, P. Rembold, S. Montangero, T. Calarco, M. Endres, M. Greiner, V. Vuletić, and M. D. Lukin, Science **365**, 570 (2019).

[29] G. Santarelli, C. Audoin, A. Makdissi, P. Laurent, G. J. Dick, and A. Clairon, IEEE Trans. Ultrason. Ferroelectr. Freq. Control **45**, 887 (1998).

[30] T. Kessler, C. Hagemann, C. Grebing, T. Legero, U. Sterr, F. Riehle, M. J. Martin, L. Chen, and J. Ye, Nat. Photon **6**, 687 (2012).

[31] D. G. Matei, T. Legero, S. Häfner, C. Grebing, R. Weyrich, W. Zhang, L. Sonderhouse, J. M. Robinson, J. Ye, F. Riehle, and U. Sterr, Phys. Rev. Lett. **118**, 263202 (2017).

[32] E. Oelker, R. B. Hutson, C. J. Kennedy, L. Sonderhouse, T. Bothwell, A. Goban, D. Kedar, C. Sanner, J. M. Robinson, G. E. Marti, D. G. Matei, T. Legero, M. Giunta, R. Holzwarth, F. Riehle, U. Sterr, and J. Ye, Nat. Photon. **13**, 714 (2019).

[33] M. Takamoto, I. Ushijima, N. Ohmae, T. Yahagi, K. Kokado, H. Shinkai, and H. Katori, Nat. Photon. **14**, 411 (2020).

[34] M. Takamoto, T. Takano, and H. Katori, Nat. Photon **5**, 288 (2011).

[35] M. H. Schleier-Smith, I. D. Leroux, and V. Vuletić, Phys. Rev. A **81**, 021804(R) (2010).

[36] D. Yu, J. Chen, and S. Zhang, Phys. Rev. A **107**, 043120 (2023).

[37] J. L. Siegel, W. F. McGrew, Y. S. Hassan, C.-C. Chen, K. Beloy, T. Grogan, X. Zhang, and A. D. Ludlow, Phys. Rev. Lett. **132**, 133201 (2024).

[38] M.-J. Yin, X.-T. Lu, T. Li, J.-J. Xia, T. Wang, X.-F. Zhang, and H. Chang, Phys. Rev. Lett. **128**, 073603 (2022).

[39] R. B. Hutson, A. Goban, G. E. Marti, L. Sonderhouse, C. Sanner, and J. Ye, Phys. Rev. Lett. **123**, 123401 (2019).

[40] N. D. Lemke, A. D. Ludlow, Z. W. Barber, T. M. Fortier, S. A. Diddams, Y. Jiang, S. R. Jefferts, T. P. Heavner, T. E. Parker, and C. W. Oates, Phys. Rev. Lett. **103**, 063001 (2009).

[41] H. Katori, M. Takamoto, V. G. Pal'chikov, and V. D. Ovsiannikov, Phys. Rev. Lett. **91**, 173005 (2003).

[42] T. L. Nicholson, S. L. Campbell, R. B. Hutson, G. E. Marti, B. J. Bloom, R. L. McNally, W. Zhang, M. D. Barrett, M. S. Safronova, G. F. Strouse, W. L. Tew, and J. Ye, Nat. Commun. **6**, 6896 (2015).

[43] X. Zhang, K. Beloy, Y. S. Hassan, W. F. McGrew, C.-C. Chen, J. L. Siegel, T Grogan, and A. D. Ludlow, Phys. Rev. Lett. **129**, 113202 (2022).

[44] J. A. Sherman, N. D. Lemke, N. Hinkley, M. Pizzocaro, R. W. Fox, A. D. Ludlow, and C. W. Oates, Phys. Rev. Lett. **108**, 153002 (2012).

[45] K. Beloy, N. Hinkley, N. B. Phillips, J. A. Sherman, M. Schioppo, J. Lehman, A. Feldman, L. M. Hanssen, C. W. Oates, and A. D. Ludlow, Phys. Rev. Lett. **113**, 260801 (2014).

[46] A. M. Rey, A. V. Gorshkov, and C. Rubbo, Phys. Rev. Lett. **103**, 260402 (2009).

[47] M. D. Swallows, M. Bishof, Y. Lin, S. Blatt, M. J. Martin, A. M. Rey, and J. Ye, Science **331**, 1043 (2011).

[48] D. Yu, Phys. Rev. A **85**, 032705 (2012).

[49] N. D. Lemke, J. von Stecher, J. A. Sherman, A. M. Rey, C. W. Oates, and A. D. Ludlow, Phys. Rev. Lett. **107**, 103902 (2011).
[50] A. D. Ludlow, N. D. Lemke, J. A. Sherman, C. W. Oates, G. Quéméner, J. von Stecher, and A. M. Rey, Phys. Rev. A **84**, 052724 (2011).
[51] S. Okaba, D. Yu, L. Vincetti, F. Benabid, and H. Katori, Commun. Phys. **2**, 136 (2019).
[52] W. Zhang, J. M. Robinson, L. Sonderhouse, E. Oelker, C. Benko, J. L. Hall, T. Legero, D. G. Matei, F. Riehle, U. Sterr, and J. Ye, Phys. Rev. Lett. **119**, 243601 (2017).
[53] J. M. Robinson, E. Oelker, W. R. Milner, W. Zhang, T. Legero, D. G. Matei, F. Riehle, U. Sterr, and J. Ye, Optica **6**, 240 (2019).
[54] M. Schioppo, R. C. Brown, W. F. McGrew, N. Hinkley, R. J. Fasano, K. Beloy, T. H. Yoon, G. Milani, D. Nicolodi, J. A. Sherman, N. B. Phillips, C. W. Oates, and A. D. Ludlow, Nat. Photon **11**, 48 (2017).
[55] S. Colombo, E. Pedrozo-Peñafiel, A. F. Adiyatullin, Z. Li, E. Mendez, C. Shu, and V. Vuletić, Nat. Phys. **18**, 925 (2022).
[56] Z. Li, S. Colombo, C. Shu, G. Velez, S. Pilatowsky-Cameo, R. Schmied, S. Choi, M. Lukin, E. Pedrozo-Peñafiel, and V. Vuletić, Science **380**, 1381 (2023).
[57] P. Lemonde and P. Wolf, Phys. Rev. A **72**, 033409 (2005).
[58] V. D. Ovsiannikov, V. G. Pal'chikov, A. V. Taichenachev, V. I. Yudin, and H. Katori, Phys. Rev. A **88**, 013405 (2013).
[59] H. Katori, V. D. Ovsiannikov, S. I. Marmo, and V. G. Palchikov, Phys. Rev. A **91**, 052503 (2015).
[60] V. D. Ovsiannikov, S. I. Marmo, V. G. Palchikov, and H. Katori, Phys. Rev. A **93**, 043420 (2016).